JGR Oceans

Upwelling of Atlantic Water in Barrow Canyon, Chukchi Sea

Shutong Li[1,2,3] ![ORCID], **Peigen Lin**[4] ![ORCID], **Tingfeng Dou**[2] ![ORCID], **Cunde Xiao**[5] ![ORCID], **Motoyo Itoh**[6], **Takashi Kikuchi**[6] ![ORCID], and **Dahe Qin**[1,2]

[1]State Key Laboratory of Cryospheric Science, Northwest Institute of Eco-Environment and Resources, Chinese Academy of Sciences, Lanzhou, China, [2]College of Resources and Environment, University of Chinese Academy of Sciences, Beijing, China, [3]School of Atmospheric Sciences, Chengdu University of Information Technology, Chengdu, China, [4]Woods Hole Oceanographic Institution, Woods Hole, MA, USA, [5]State Key Laboratory of Earth Surface Processes and Resource Ecology, Beijing Normal University, Beijing, China, [6]Institute of Arctic Climate and Environment Research, Japan Agency for Marine-Earth Science and Technology, Yokosuka, Japan

Abstract Using long-term moorings data together with wind and sea ice measurements, we document the characteristics and variations of upwelling in Barrow Canyon and investigate the upwelled Atlantic Water (AW) on the Chukchi Sea shelf and how it impacts the ice cover. Driven by strong northeasterly winds, upwelling occurs more often in the cold months, and the occurrence tends to increase interannually since 2001. Over the 12-year mooring record at the mouth of Barrow Canyon, roughly 10% of the upwelling events can drive AW onto the Chukchi Sea shelf. Both AW and non-AW upwelling events have more occurrence and stronger strength in the cold months, but do not present a significant interannual trend. These variations are associated with the northeasterly winds. Comparing to the non-AW upwelling, the AW upwelling is generally characterized by more vertical displacement of the AW layer at the mouth of Barrow Canyon, and stronger up-canyon volume and heat transport. In the ice-covered period, these two types of upwelling have different consequences for forming polynyas on the shelf. Under similar wind forcing, the ice reduction appears confined in the coastal region in the non-AW upwelling events, while during AW upwelling events, the sea ice declines dramatically in the shelf interior with 15% more ice loss. It elucidates that the heat carried by the upwelled AW plays a considerable role in modulating the ice cover in the shelf interior.

Plain Language Summary Upwelling in Barrow Canyon brings heat and nutrients that can affect sea ice condition and ecosystems on the Chukchi Sea shelf. In this study, we use mooring data in the vicinity of Barrow Canyon together with the wind data and satellite ice concentration data, to investigate the characteristics and variations of upwelling in the canyon, and how the upwelled warm Atlantic Water (AW) modulates the ice cover on the shelf. Driven by the strong northeasterly winds, the upwelling in the canyon is characterized by an up-canyon flow and uplifting of water masses, and the upwelling occurrence varies seasonally and interannually. Roughly 10% of the events can upwell the AW onto the Chukchi Sea shelf, which mainly occur in the cold months when the strong northeasterly winds blow. Under similar wind forcing, upwelling of AW leads to the significant ice decrease in the shelf interior, while non-AW upwelling causes less ice loss that is confined along the coastal region. These discrepancies suggest that the extra heat brought by the AW upwelling in the Barrow Canyon can result in a significant ice loss in the interior of the Chukchi Sea shelf.

1. Introduction

Pacific-origin water flows into Arctic through Bering Strait with the mean transport of 1.0 ± 0.05 Sv (Woodgate, 2018), carrying significant freshwater, heat, and biogeochemical properties. The Pacific-origin water propagates northward mainly via three pathways (Figure 1): Western pathway which passes through Herald Canyon; Central Channel pathway flows through the channel between Herald Shoal and Hanna Shoal; and Alaskan Coastal Current (ACC) flows against the coast of Alaska (Lin, Pickart, Mcraven, et al., 2019; Weingartner et al., 2005). The Central Channel pathway flows anticyclonically around Hanna Shoal with bifurcations prior to arriving Hanna Shoal. These branches of the Central Channel pathway ultimately join into the ACC at the head of Barrow Canyon and drain off the shelf through Barrow Canyon (Lin, Pickart, Mcraven, et al., 2019). The mean transport of the outflow through Barrow Canyon is 0.44 ± 0.07 Sv (Itoh et al., 2013), and often exceeds 1 Sv in summer (Gong & Pickart, 2016; Itoh et al., 2015). As such, Barrow Canyon, where the nutrient-rich Pacific Water converges, is one of the important biological "hotspots" in the Chukchi Sea (Grebmeier et al., 2006, 2015). Pickart et al. (2021) revealed that the flow accelerates as converging into the canyon, resulting in a strong downwelling on
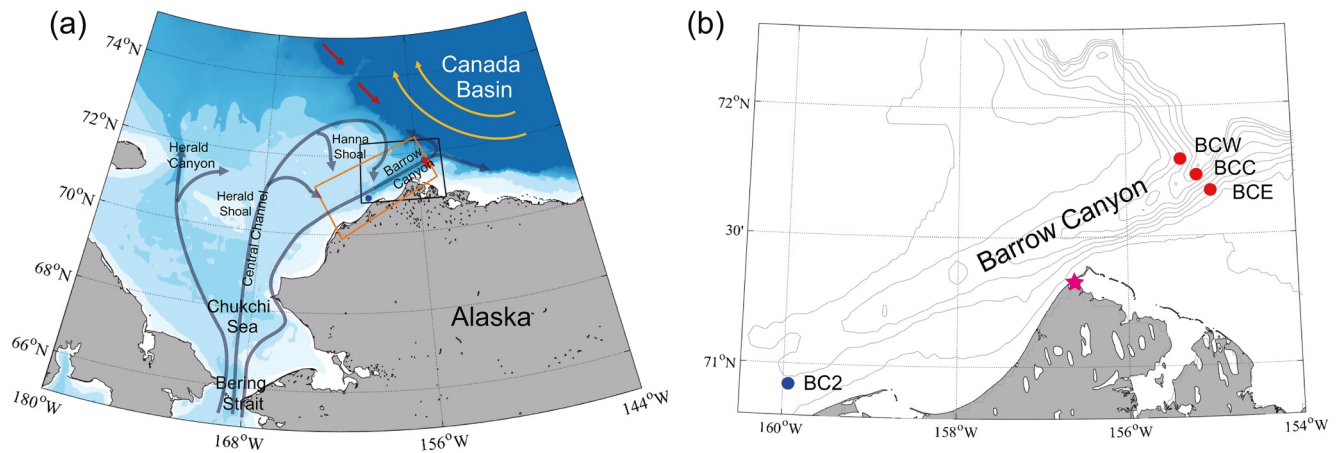
Figure 1. (a) Schematic circulation of the Chukchi and western Beaufort Seas. The blue and red arrows represent the circulation of Pacific-origin water and the boundary current of Atlantic-origin water, and the yellow arrows denote the Beaufort Gyre. The locations of moorings near the mouth and head of Barrow Canyon are denoted by red and blue dots, respectively. The blue box denotes the study region shown in (b). The orange box is the region over which the ice concentration is averaged. The bathymetry is from ETOPO2v2 (National Geophysical Data Center, 2006). (b) Enlarged view of the study region in the vicinity of Barrow Canyon. The magenta star marks the location of the Utqiaġvik meteorological station.

this cyclonic side (northwestern side) of the flow. The downwelling feeds the biological processes to the seabed and thus contributes a benthic "hotspot" in the Barrow Canyon. Under strong northeasterly winds, the Barrow Canyon outflow can be reversed toward up-canyon (Lin, Pickart, Mcraven, et al., 2019), along with upwelling in the canyon (Pisareva et al., 2019).

Warm and salty Atlantic Water (AW) flows into Arctic through Fram Strait and Barents Sea, and circulates cyclonically along the continental slope (Aksenov et al., 2011). It negotiates the Chukchi Borderland via multiple routes and eventually has two branches approaching the southern Canada Basin (Li et al., 2020). In the western Arctic, the AW resides beneath the Pacific Water layer, with the mean interface at ~150 m depth on the continental slope (Nikolopoulos et al., 2009), which deepens to the deep basin. In addition to the Atlantic- and Pacific-origin water masses, the fresh sea-ice melt water/meteoric water (including precipitation and river runoff) lies at the surface (Lin et al., 2020).

Upwelling plays an essential role in the shelf-basin exchanges of freshwater, heat and biogeochemical properties in the western Arctic, which have significant impacts on the halocline, sea ice and ecosystem in the basin (Macdonald et al., 1987; Pickart et al., 2011; Proshutinsky et al., 2009). In the Alaskan Beaufort Sea, four to five episodic upwelling events can fulfill the annual nitrate budget in the Alaskan Beaufort Sea (Pickart, Spall, & Mathis, 2013). The upwelling is mainly driven by easterly winds, dictated by the two atmospheric centers of action—the Aleutian Low and the Beaufort High (Pickart, Schulze, et al., 2013). Associated with the seasonality of the along-coast wind, the wind-driven upwelling is intensified in the spring and fall (Lin et al., 2016). Using 2 years of mooring data Schulze and Pickart (2012) demonstrated that upwelling in the Alaskan Beaufort Sea takes place throughout the year regardless of the ice presence (as long as the ice is mobile), although the upwelling can be enhanced via the ice-ocean stress when there is partial ice cover. The effect of ice on upwelling has also been shown in the Canadian Beaufort Sea (Lin et al., 2020). Lin, Pickart, Moore, et al. (2019) identified 115 upwelling events within a 6-year period, one third of them brings only Pacific Water onto the shelf, occurring in the warm months. The remaining two thirds uplift AW mainly in the cold months. They argued that the primary driving factor is the seasonal variation of the Pacific Water-AW interface depth, which is modulated by the local wind stress curl.

Upwelling also commonly occurs in the Barrow Canyon. Unlike the canonical coastal upwelling associated with the secondary circulation, this is the process that the water is carried by the reversed Barrow Canyon outflow up to the shelf. The upwelling is mainly driven by northeasterly winds (Carmack & Kulikov, 1998; Okkonen et al., 2009; Pisareva et al., 2019), and eastward-propagating shelf waves can also play a role (Aagaard & Roach, 1990). Using the data from a mooring situated near the head of the canyon, Pisareva et al. (2019) found a good correlation between the strength of upwelling and the along-coast wind, suggesting that stronger northeasterly winds can

lead to stronger upwelling in the canyon. The upwelling in Barrow Canyon more often brings Pacific Water, but upwelling of AW is rare. Pisareva et al. (2019) found 5 AW events in a 2-year mooring record near the head of the canyon. Using the moorings on the Chukchi Sea shelf in 2010–2015, Ladd et al. (2016) found eight upwelling events bringing the warm AW to the interior of the shelf. These AW upwelling events can lead to the formation and development of polynyas on the shelf. The evidence of ice melted by the upwelled AW was also revealed by Hirano et al. (2018) using numerical model and mooring data. They pointed out that there are mainly two mechanisms of the polynya formation —the divergence due to the strong northeasterly wind and the oceanic heating beneath the ice—which however are difficultly distinguished. This is consistent with the results of Hirano et al (2016), who suggested that the polynya near the coast of Barrow Canyon is a hybrid polynya, formed by both wind-driven divergence of ice and sensible heat due to upwelling.

The upwelling also modifies the nutrient concentrations on the Chukchi Sea shelf (Beaird et al., 2020; Ladd et al., 2016). Both the Pacific Water (particularly Pacific Winter Water) and warm AW, containing high levels of nutrients, are upwelled to the shelf and contribute to the biological processes (Lin, Pickart, Mcraven, et al., 2019; Pickart et al., 2019). Meanwhile, the upwelled waters generate an unstable gravity current that triggers strong vertical mixing, which allows the nutrients to reach to the upper layer (Beaird et al., 2020).

In this study, using the data from the moorings at the mouth and head of the canyon, we aim to address the characteristics and variations of upwelling events in the Barrow Canyon, particularly the ones carrying AW onto the shelf, and classify the effects of wind and sensible heat on the reduction of ice during the upwelling events. The study is organized as follows. We begin with a description of the moorings, ice concentration and atmospheric data, and the methods in light of the calculations of the upwelling and wind strengths and the oceanic heat transport (Section 2). After identifying the upwelling events based on the mooring data, we investigate the variation of the events and the effect of wind (Section 3). We then compare the nature and forcing of AW upwelling and non-AW upwelling in Section 4. Lastly, we address the impacts of both types of upwelling on ice cover on the shelf and distinguish the effects of oceanic heat and wind divergence on the polynya formation (Section 5). We end by discussing the uncertainties and summarizing the results (Sections 6 and 7).

2. Data and Methods

2.1. Mooring Data

At the mouth of Barrow Canyon, we use the data from three moorings deployed from 2001 to 2017 provided by the Japan Agency for Marine-Earth Science and Technology (JAMSTEC; red dots in Figure 1). One mooring is located in the center of Barrow Canyon (BCC), and the others are situated on the eastern and western flanks of the canyon (BCE and BCW). All moorings were equipped with MicroCATs providing hourly data of temperature, salinity and pressure, and Acoustic Doppler Current Profilers (ADCPs) measuring velocity profiles with a bin size of 4–8 m and a sampling interval of 0.25–2 hr. The exception is that the shoulder moorings (BCE and BCW) were equipped with current meters instead of the ADCPs in some earlier years (Table 1).

The drifts in the sensors over 1 year were 0.001°C for temperature and 0.01 for salinity, and accuracy for velocity measurements was better than or equal to 1 cm s^{-1} (Itoh et al., 2012). Following the method of Itoh et al. (2013), temperature, salinity and velocity data were also linearly interpolated to a 1 m fixed vertical grid, and the values at the shallowest observational level were extended to the surface. At the mooring BCC, the MicroCAT at 50 m failed from September 2002 to September 2003: for this period, we used the hydrographic data averaged between the two shoulder moorings BCE and BCW. The velocity at BCE was used to compensate the failure of the mooring BCC's ADCP in the year of September 2002 to September 2003. Nonetheless, there were still some gap years, June 2004 to September 2005, September 2008 to August 2010, and October 2013 to August 2014 (see Table 1). After these data processing, the velocity timeseries were de-tided using the T-Tide harmonic analysis toolbox (Pawlowicz et al., 2002). We compute the velocity components in the along-stream (56°T, positive down-canyon) and cross-stream (326°T) coordinate (Pisareva et al., 2019).

At the head of the canyon, we use the 4-year hydrographic data near the bottom at the mooring (BC2) from 2010 to 2015 (Weingartner et al., 2017; blue dot in Figure 1) to examine whether AW is transported onto the shelf. The bottom MicroCAT collected the data every 15 min (Table 1).

Table 1
Information of the Moorings Near the Mouth (BCC, BCE, and BCW) and Head (BC2) of Barrow Canyon

Mooring ID	Lat (°N)	Lon (°W)	Bottom depth (m)	Date range	ADCP Effective range (m)	Sample Int. (h)	Vertical Res. (m)	MicroCAT Depth (m)	Sample Int. (h)
BCC	71°44.01'	155°09.55'	285	30 September 2001–9 September 2002	10–285	1	4	53, 93, 133, 192, 256	1
				9 September 2002–10 March 2003	10–285	1	4	90, 252	1
				6 October 2003–21 June 2004	10–250	2	8	44, 84, 123	1
				02 October 2005–1 October 2006	10–250	2	8	40, 77, 116, 173, 266	1
				02 October 2006–31 August 2008	10–285	2	4	38, 74, 114, 173, 265	1
				11 September 2010–5 September 2013	10–285	2	4	42, 81, 119, 179, 268	1
				13 September 2014–9 September 2015	10–285	2	4	44, 84, 122,153, 182, 253, 271	1
				10 September 2015–5 September 2016	10–285	2	4	44, 84, 123, 152, 272	1
				6 September 2016–6 September 2017	10–285	1	4	43, 83, 119,147, 178, 250, 270	1
BCE	71°40.35'	154°59.74'	106	30 September 2001–9 September 2002	10–75	0.25	4	48, 89	1
				09 September 2002–5 October 2003	10–75	1	4	52, 86	1
				05 October 2003–9 September 2008	45, 70[a]	2	–	35, 90	1
				12 September 2010–9 September 2013	10–75	2	4	42, 91	1
				12 September 2014–5 September 2016	10–75	2	4	39, 93	1
				7 September 2016–6 September 2017	10–75	1	4	39, 93	1
BCW	71°47.74'	155°20.75'	170	1 October 2001–8 September 2002	10–140	1	4	41, 80, 160	1
				9 September 2002–5 October 2003	10–140	1	4	52, 82, 152	1
				6 October 2003–2 October 2005	50, 80, 140[a]	2	–	30, 157	1
				2 October 2005–9 September 2008	50, 80, 140[a]	2	–	40, 115, 151	1
				29 September 2010–25 September 2012	50, 90, 140[a]	2	–	35, 113, 150	1
				27 September 2012–05 September 2013	10–140	2	4	40, 90, 120, 155	1
				13 September 2014–5 September 2016	10–140	2	4	43, 88, 122, 156	1
				6 September 2016–9 September 2017	10–140	1	4	40, 120, 155	1
BC2	70°55'	159°55'	52	17 August 2010–10 August 2015	–	–	–	50	0.25

Note. ADCP: Acoustic Doppler Current Profiler.
[a]only current meters.

2.2. Wind Data

The 10-m wind data were obtained from the meteorological station at Utqiaġvik, Alaska (magenta star in Figure 1b). The data well represent the regional wind condition in the vicinity of Barrow Canyon (Pickart et al., 2019, 2021). The data have been quality controlled and interpolated onto an hourly interval (see Pickart, Schulze, et al., 2013 for the details). In this study we consider the along-coast wind (52°T, Pisareva et al., 2019) which plays an essential role in the outflow and upwelling in Barrow Canyon (Pisareva et al., 2019; Weingartner et al., 2017).

2.3. Ice Concentration Data

We also employed the Advanced Very High Resolution Radiometer (AVHRR) sea ice concentration (SIC) products spanning from 2001 to 2017, obtained from the National Climate Data Center of the National Oceanic and Atmospheric Administration. This is a daily data set with a spatial resolution of 0.25°, and has been developed using optimum interpolation which fills in gaps due to low-level clouds (Reynolds et al., 2007). The mean sea ice

concentration was computed within the orange box in Figure 1, covering the coastal region including the Barrow Canyon.

2.4. Definition of Upwelling

Using a mooring at the head of Barrow Canyon (close to the BC2), Pisareva et al. (2019) defined the upwelling events based on velocity and wind. In this study we applied these criteria to the long-term record of the mooring BCC at the mouth of the canyon. In particular, we first computed the timeseries of the depth-averaged along-stream velocity (within the ADCP range of 10–250 m), and then identified upwelling periods when the along-stream velocity is negative (Barrow Canyon outflow is reversed toward up-canyon). The response of the flow lags the onset of winds by 6 hr, close to the delay time reported by Pisareva et al. (2019) in the head of Barrow Canyon (9 hr) and Lin, Pickart, Moore, et al. (2019) in the western Beaufort Sea (8 hr). Taking account of the delay time, we computed the mean along-coast wind for each of above-identified upwelling events. Here we consider the events when the mean along-coast wind is negative (northeasterly wind). Events apart less than 1 day are combined as one event, and events with the duration less than 1 day are removed. The results are not sensitive to the thresholds. As such, over the 12-year record at BCC, we identified 328 upwelling events in total (see Table S1 for details).

To quantify the strength of each upwelling, we defined an upwelling index (UI) as

$$\text{UI} = |\int_{t_s}^{t_e} U_c \, dt|, \tag{1}$$

where U_c is vertically averaged along-stream velocity at BCC and t_s and t_e are the start and end times for each event. The index accounts for the magnitude and duration of upwelling, in the unit of m s^{-1} day. We take the absolute value of the index.

2.5. Wind Index

To address how wind modulates the upwelling, Lin, Pickart, Moore, et al. (2019) used the cumulated Ekman transport. Similarly, here we employed the cumulated along-coast wind speed during each upwelling event as a wind index (WI), in the same unit as the UI,

$$\text{WI} = |\int_{t_s-t_d}^{t_e-t_d} u_{\text{wind}} \, dt|, \tag{2}$$

where u_{wind} is the along-coast wind, t_d is the delay time. Consistent with the UI, the absolute value of WI is used.

2.6. Up-Canyon Fluxed Heat

Using the all of the three moorings at the mouth of the Barrow Canyon, we computed the amount of the oceanic heat (*H,* Joules) that is transported up-canyon during each upwelling event,

$$H = |\int_{t_s}^{t_e} \int_A u_c \rho \, (\theta - \theta_0) \, C_p \, dA \, dt|, \tag{3}$$

where u_c is the depth-dependent along-canyon velocity, ρ is the potential density, θ is the potential temperature, and C_p is the specific heat of seawater. The reference temperature θ_0 is set to the freezing point of Bering Strait waters, $-1.91°C$ (for salinity of 33.5). A is the cross-sectional area of the current, with the vertical range from 1 to 120 m. This layer is within the PW layer where the AW often reaches during upwelling, and in which the advected heat more likely affects the ice on the shelf (the result is not sensitive to the vertical range). We would note that the heat calculation can have considerable errors due to the coarsely spaced moorings. The average error for heat flux is 3%–16% of the total flux depending on the resolution of the original data (Itoh et al., 2013).
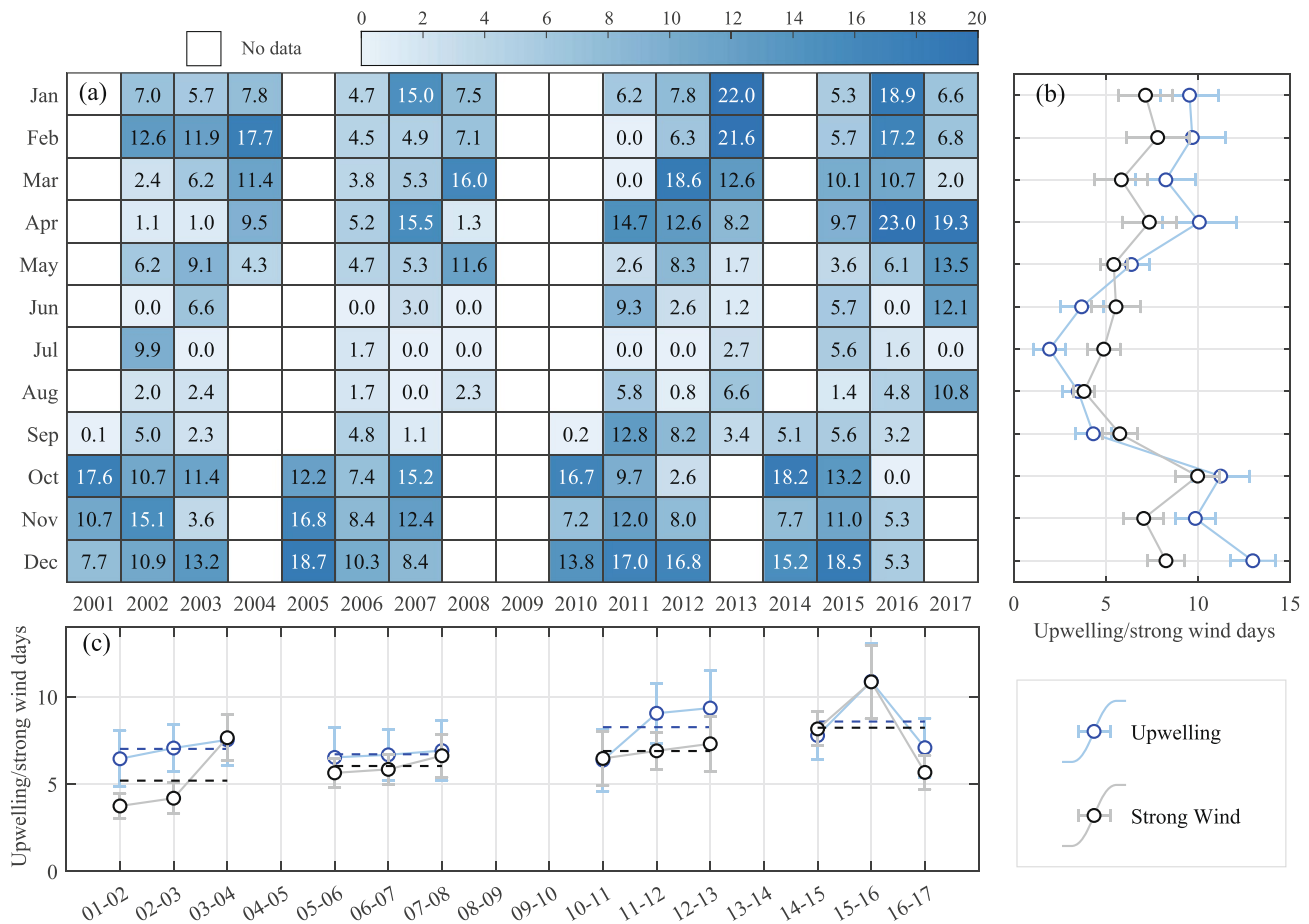
Figure 2. (a) Upwelling days in each month from 2001 to 2017 (color). Missing values are in white. (b) Seasonal and (c) interannual variations of the monthly upwelling days (blue curve) and strong wind days (black curve). The horizontal dashed lines in (c) are the mean upwelling (blue) and strong wind (>5.0 m s^{-1}, black) days of each three-year segment. The errorbars denote standard errors.

3. Barrow Canyon Upwelling Events

3.1. Occurrence of Upwelling

The mean duration of the 328 upwelling events is 3.3 days, shorter than the 4.8 days that Lin, Pickart, Moore, et al. (2019) found for upwelling events in the western Beaufort Sea. The discrepancy may be due to the different upwelling definitions (velocity vs. potential density anomaly) and the more energetic flow in the mouth of Barrow Canyon. To address the occurrence of upwelling, we summed up the upwelling days in each month of the year when the data were available (Figure 2a). One sees that upwelling has a low occurrence in the warm months, while in the cold months it frequently occurs for more than half a month, with a peak of 23 days in April, 2016. To shed light on this seasonality, we computed the monthly mean of the upwelling days (blue curve in Figure 2b). It shows that the upwelling occurrence is a minimum in July, while peaks in April and in October–December, which is consistent with the variation in the western Beaufort Sea (Lin, Pickart, Moore, et al., 2019).

Pickart, Schulze, et al. (2013) suggested that the number of upwelling events in the Alaskan Beaufort Sea has increased from the 1990s to 2010. To investigate the long-term variation of upwelling in Barrow Canyon, we averaged the monthly upwelling days for each available year (from September to the next August, Figure 2c). The upwelling days in the month without available data were filled up using the climatological mean of this month over the years. This shows an overall increase from 7.0 ± 0.8 days in the early years to 8.6 ± 1.0 days in the recent years.
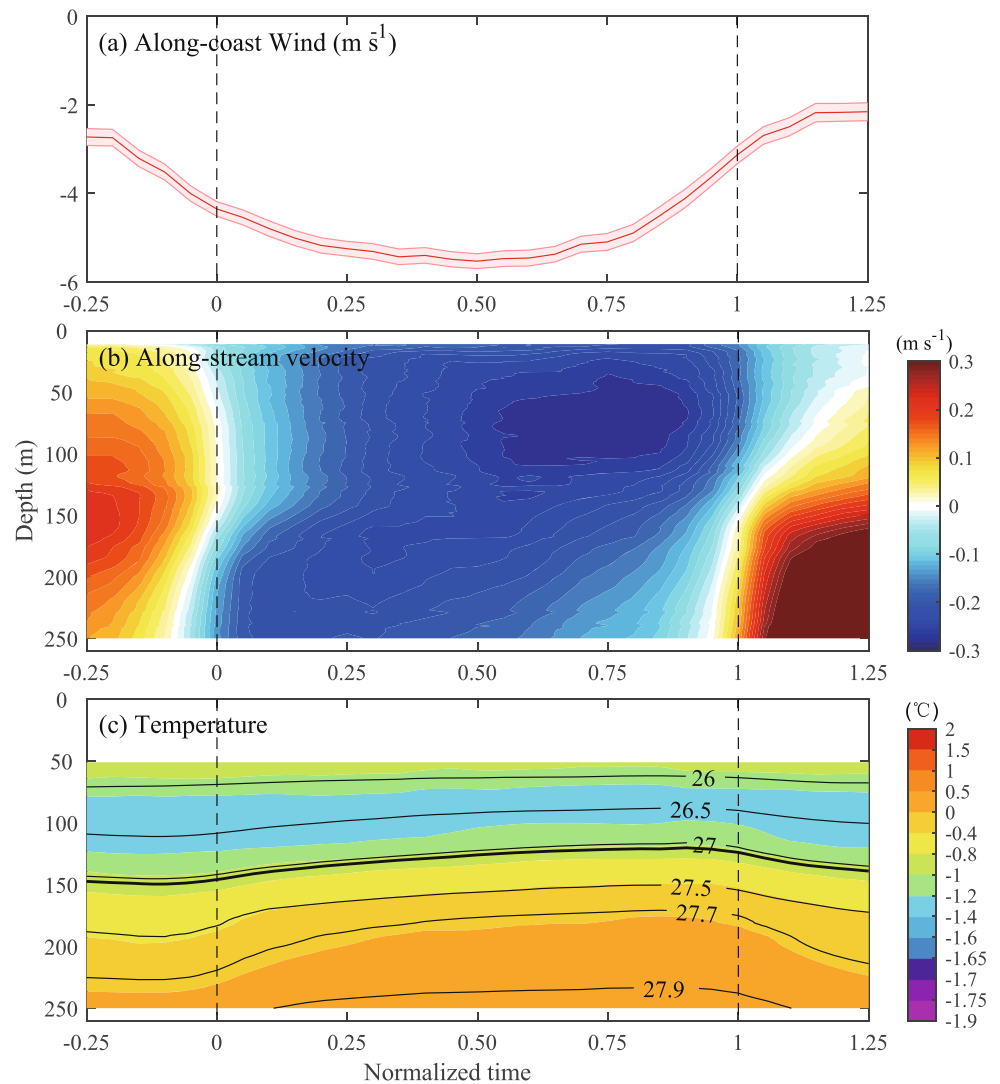
Figure 3. Composite upwelling event constructed from the 328 individual events. (a) The along-coast wind speed (m s^{-1}) where negative is northeasterly. The shading represents standard error. (b) Depth-dependence along-stream velocity (m s^{-1}) where negative is up-canyon. (c) Potential temperature (°C) overlain by the isopycnals (kg m^{-3}). The thick contour represents the interface of Pacific Water and Atlantic Water (27.06 kg m^{-3} isopycnal, Nikolopoulos et al., 2009).

3.2. Evolution of a Composite Upwelling Event

To evaluate the general features of upwelling, we defined a normalized time (t_n), with $t_n = 0$ ($t_n = 1$) corresponding to the onset (end) of the event. Averaging the 328 individual events we constructed a composite event during $t_n = -0.25$–1.25 considering the pre- and post-condition of the event (Figure 3). The composite of the depth-dependent along-stream velocity reveals that the flow is intensified in the middle layer (~150 m) prior to the onset of upwelling (Figure 3b). At the onset of upwelling, the flow is reversed, and becomes subsurface-intensified in the late event peaking at −0.28 m s^{-1} near 75 m depth around $t_n = 0.75$. As the upwelling ends, the down-canyon flow is enhanced in the lower layer, stronger than the initial condition, although the negative velocities last longer in the upper layer, consistent with the observations in Beaird et al. (2020). This is likely the signature of the rebound jet induced by the combined effect of the fast barotropic adjustment and slow baroclinic adjustment (Li et al., 2021; Lin, Pickart, Moore, et al., 2019; Pickart et al., 2011).

The precondition of hydrography is that the cold Pacific Water is located above the warm AW with the interface (isopycnal of 27.06 kg m^{-3}) at 150 m (Figure 3c), in line with the annual-mean depth of the interface measured in the Beaufort Sea (Nikolopoulos et al., 2009). Associate with the reversed flow during upwelling, the AW layer

is lifted and reaches the shallowest depth at ∼120 m at $t_n = 0.9$, later than the velocity peak. It is understandable that the hydrographic field has a longer lag response to the wind (Lin, Pickart, Moore, et al., 2019). It relaxes to the initial level as the upwelling ends.

3.3. Effect of Wind

Pisareva et al. (2019) has demonstrated the effect of wind on the seasonality and individual events in 2002–2004. It is of interest to investigate the effect of wind on the upwelling at the mouth of the canyon in a longer timescale. Applying the same method of computing the upwelling days above, for each month of the year when the mooring data were available, we count the number of the days when the along-coast wind is stronger than the mean wind speed during upwelling events, 5.0 m s^{-1}, consistent with the wind thresholds in Pisareva et al. (2019) and Lin et al. (2021).

The monthly values are averaged for each month of the year and also for each year. Figure 2b reveals that in terms of the seasonality, the number of the strong wind days is well correlated with the upwelling days ($R = 0.78$, $p < 0.01$). Similarly, strong winds occur more frequently in cold months than that in the warm months—two peaks in spring and fall. Interestingly, the strong wind days is slightly less than the upwelling days in the cold months. We argue that it may be due to the stronger upwelling in the cold months takes longer to relax, and the weaker coastal current in the cold month can be more easily reversed (Itoh et al., 2013). The good correlation is also found in the interannual variation (Figure 2c). The strong wind days significantly increase from 5.2 ± 1.5 days in 2001–2004 to 8.2 ± 0.8 days in 2014–2017, which is in the line with the increase trend of upwelling days.

How does the wind vary during upwelling? To answer this, we constructed the composite of the along-coast wind in the normalized time (Figure 3a). On average the northeasterly wind is weak and gradually strengthens prior to the onset of upwelling. Remind that as the exist of the outflow in Barrow Canyon, the occurrence of upwelling requires a strong northeasterly wind (Lin et al., 2021; Pisareva et al., 2019). The wind speed reaches to the peak right after the middle of the event, but before the velocity peak. It then dies out quickly to the end, consistent with the asymmetric variations of velocity and hydrographic fields.

Having shown that upwelling is strongly related to wind, we further quantify the wind effect by regressing the UI with wind index (WI; see Section 2) for all of the identified upwelling events (Figure 4). Not surprisingly, it displays a good linear relation between the two indexes, with a correlation coefficient $R = 0.75$ ($p < 0.01$). It suggests that stronger northeasterly wind event (higher WI) can result in more intense upwelling in Barrow Canyon. There are a few outliers where the strong upwelling events are associated with the relatively small WI. During each of these events, the northeasterly wind occasionally drops and reverses. Such temporary wind variations were not able to terminate an upwelling, but decrease the WI.

## 4. AW Upwelling Versus Non-AW Upwelling

As mentioned above, only a few upwelling events in Barrow Canyon can bring AW onto the shelf (referred to as AW upwelling), while most of them transport Pacific Water (referred to as non-AW upwelling below), consistant with the previous studies (Ladd et al., 2016; Pisareva et al., 2019). It motivates us to characterize the AW upwelling versus the non-AW upwelling in the long record. Following Nikolopoulos et al. (2009) and many other studies, AW is considered as the water with a temperature higher than −1.26°C and a salinity over 33.64. As we stated in the data and method, the upwelling is defined using the BCC data near the mouth of the canyon. Using this single mooring, however, we cannot ensure whether the AW is advected onto the shelf during a given upwelling. We thus also employ the 4-year bottom hydrographic data at the mooring BC2 near the head of the canyon, spanning from 2010 to 2015 (see Section 2; Weingartner et al., 2017).

In these 4-year record, we found that 14 of 106 upwelling events occurring in the mouth of the canyon were followed by the AW signal appearing at the head of the canyon (red dots in Figure 5). On average, the first appearance of AW at the head of the canyon lags the onset of the upwelling at mooring BCC by 3.9 days. It is consistent with the advective time, 3.9–4.9 days, given the distance between the two moorings (∼170 km) and the mean up-canyon velocity ranging from −0.3 to −0.4 m s^{-1} during upwelling. Note that Ladd et al. (2016) reported 8 AW events using the mooring on the shelf in 2010–2015, while we have 10 AW events using the BC2 mooring
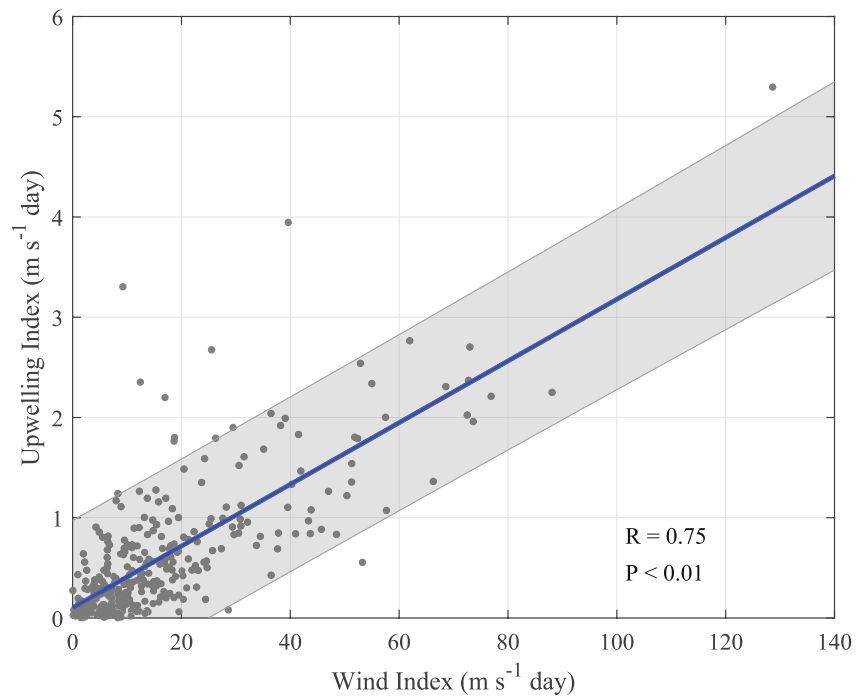
Figure 4. Upwelling index versus wind index for all upwelling events over the 12-year record. The blue line denotes the best linear fit, and the gray shading area is within the 95% confidence level.
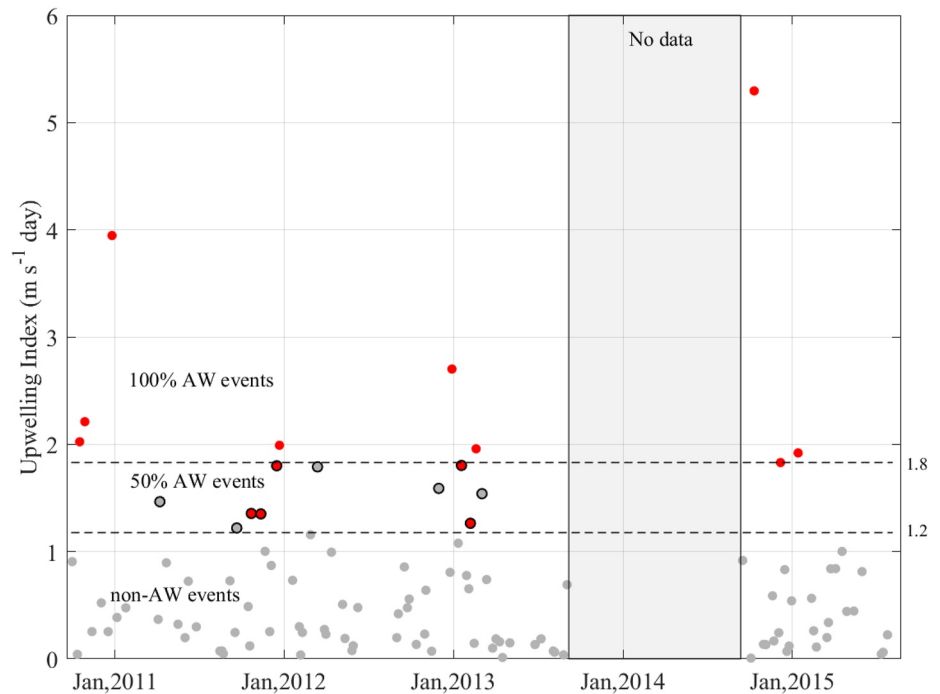
Figure 5. Upwelling index of the identified events during August, 2010 to August, 2015. The events that lead to the presence of the Atlantic Water (AW) ($T > -1.26°C$ and $S > 33.64$) at the head of the canyon are marked in red, the remaining events are in gray. The black dashed lines represent the boundaries of the AW events, non-AW events, and the 50%-chance AW events (dots with black circles). The period of no data in September, 2013 to September, 2014 is shaded.
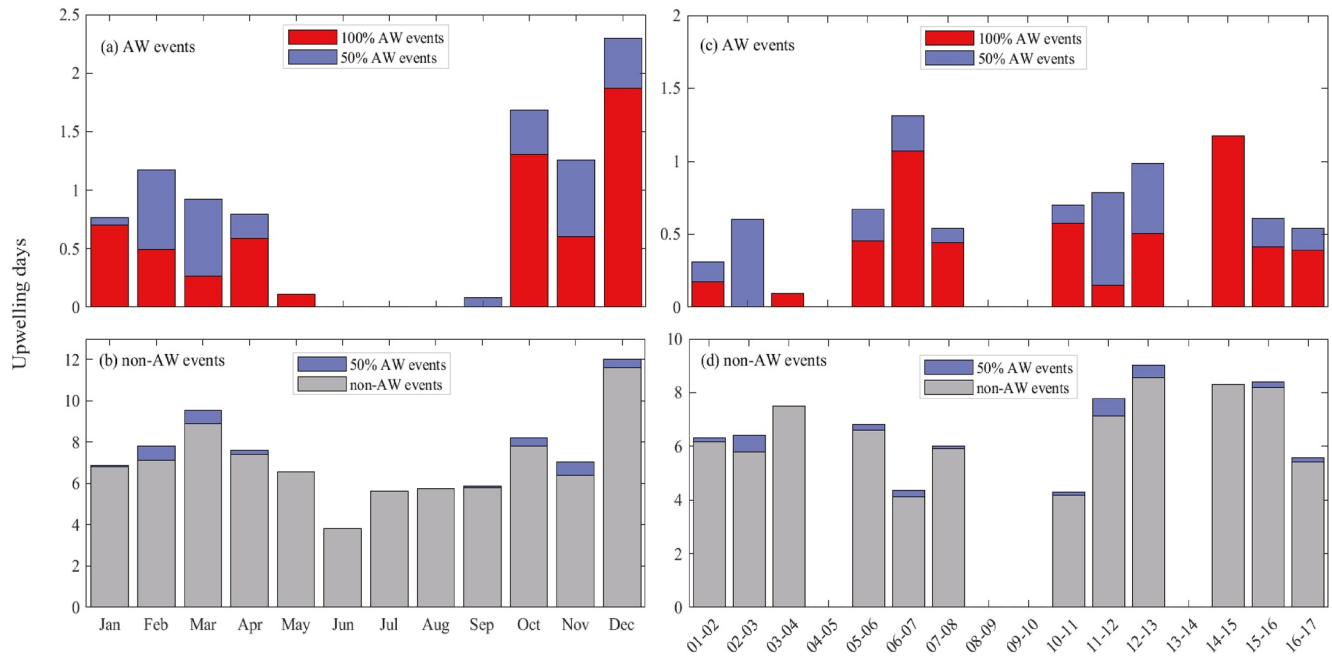
Figure 6. (a and b) Seasonal and (c and d) interannual occurrences of Atlantic Water (AW) upwelling events (red bars) and non-AW upwelling events (gray bars). Days of the 50%-chance AW upwelling events (purple bars) evenly splits to AW and non-AW upwelling days.

data during the overlapping periods of the two moorings. This discrepancy is due to their mooring located farther away from the head of the canyon.

Most of the AW events in 2010–2015 have the UI > 1.83 m s^{-1} day (Figure 5), indicating that the stronger upwelling is more likely to bring the AW to the head of the canyon. The AW upwelling accounts for 50% of the events when the UI falls in the range of 1.18–1.83 m s^{-1} day. None of the upwelling associated with AW when UI is below 1.18 m s^{-1} day. We thus apply these thresholds to all of the upwelling events in the 12-year data of the mooring BCC, and identify the AW upwelling and non-AW upwelling events.

4.1. Seasonal and Interannual Variations

Over the 12-year record, we identified 22 confirmed AW upwelling events, 283 non-AW upwelling events, and 23 events with half the chance of bringing AW ($1.18 < \text{UI} < 1.83$), accounting for 6.7%, 86.3%, and 7.0% of the total 328 upwelling events, respectively. How often these two types of upwelling occur seasonally and interannually? As our calculation for all upwelling above, we first integrate the upwelling days for each individual month and then computed the monthly mean and annual-mean (September to next August) upwelling days (Figure 6). To not underestimate the upwelling occurrence, for the 23 events with half the chance of bringing AW, we counted the half of the upwelling days to the AW upwelling and the other half to the non-AW upwelling. The monthly mean upwelling days reveal that the AW upwelling is mainly found in the cold months, and barely seen in the warm months (Figure 6a). Consistent with the previous studies, AW upwelling is rare, with the maximum occurrence of ~2 days in December. By contrast, non-AW upwelling can be found throughout the year with a similar seasonality, that is, more occurrence in cold months than warm months (Figure 6b). It ranges from 3.8 days in June to the peak of 12.0 days in December.

Consistent with the occurrence, upwelling strength (UI) also reveals a clear seasonality (Figures 7a and 7b, the 50%-chance AW upwelling events are not considered here). AW upwelling is strong from late fall through winter, with UI >2.5 m s^{-1} day, and weakens in late winter and spring. Non-AW upwelling is also strong in winter, but becomes very week in summer, particularly in July (UI < 0.1 m s^{-1} day). It is due to the weaker reversed flow and shorter duration in the warm months (not shown). We also constructed the timeseries of monthly mean WI (Figures 7a and 7b). The good agreement between WI and UI again reveals the link between upwelling and along-coast wind, although the correlation is less for AW upwelling than non-AW upwelling. We argue that the less
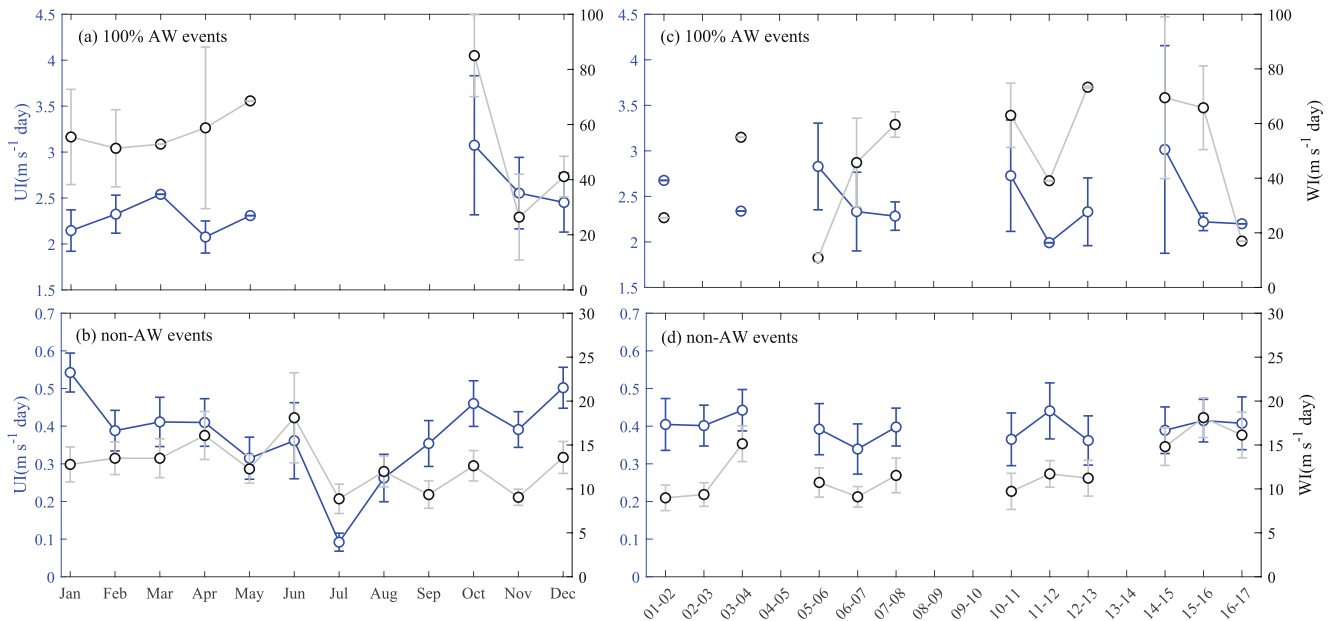
Figure 7. (a and b) Seasonal and (c and d) interannual variations of upwelling index (blue curves) and WI (black curves) of Atlantic Water (AW) upwelling events and non-AW upwelling events. The 50%-chance AW upwelling events are excluded. No error bar for the years when there was only one event.

correlation of AW upwelling strength and wind is due to the small number of the events that adds more uncertainties. It is also reflected by the larger standard errors. Note that for non-AW upwelling, the increase of WI in the cold months is not as obvious as that of UI. As we discussed above, it is likely due to the weaker outflow in Barrow Canyon can be more easily reversed in the cold months.

Both AW and non-AW upwelling occur with a clear interannual variation, but seem no correlation with each other (Figures 6c and 6d). The annual-mean AW upwelling days peak in 2006–2007 (exceed 1 day) when the non-AW upwelling becomes less frequent, while the second peak of the AW upwelling days in 2014–2015 corresponds to a high non-AW upwelling occurrence. By contrast to the overall variation (Figure 2), AW upwelling occurrence has no significantly increase trend, as well as non-AW upwelling. It is also true in terms of upwelling strength (Figures 7c and 7d). The annual mean UI varies from 2 to 3 m s^{-1} day in AW upwelling. Note that in some years the mean values were computed from very a few AW upwelling events that result in large standard errors. Non-AW upwelling is weaker and its strength varies slightly from year to year, with UI of 0.3–0.5 m s^{-1} day. Overall, the interannual variation of UI is also associated with WI.

4.2. Velocity and Hydrographic Structures

For each type of upwelling, how do along-coast winds vary during an event and how do velocity and hydrography structures respond? To address that, we computed the composite event for AW upwelling and non-AW upwelling (the 50%-chance AW events are excluded), respectively. As shown in Figure 8a, the northeasterly wind starts strengthening prior to the onset of the AW upwelling, and reaches the peak wind speed of −6.8 m s^{-1} at $t_n = 0.75$. It rapidly falls to be negligible after the event. Before the upwelling, the current is intensified in the lower layer and directed down-canyon, with a maximum velocity of 0.26 m s^{-1} at 170 m (Figure 8b). By the time of the onset of the upwelling, the current reverses to up-canyon (negative) and velocity increases gradually. The up-canyon current becomes subsurface-intensified, exceeding −0.5 m s^{-1} in the layer of 50–90 m at $t_n = 0.80$ associated with the peak along-coast wind. Meanwhile, the upper boundary of warm and salty Atlantic Water is vertically uplifted from 150 to 100 m toward the end of the event (Figures 8c and 8d). As we saw in the composite plot of all events in Figure 3, after the event, a rebound jet in the lower layer start to establish, with more than double of the initial velocity at the depth of 200 m.

During non-AW upwelling, the mean along-coast wind speed ranges from −3.6 to −5.7 m s^{-1}, with average value of −4.9 m s^{-1} (Figure 8e). The wind speed peaks immediately after the middle of the event and drops back to the
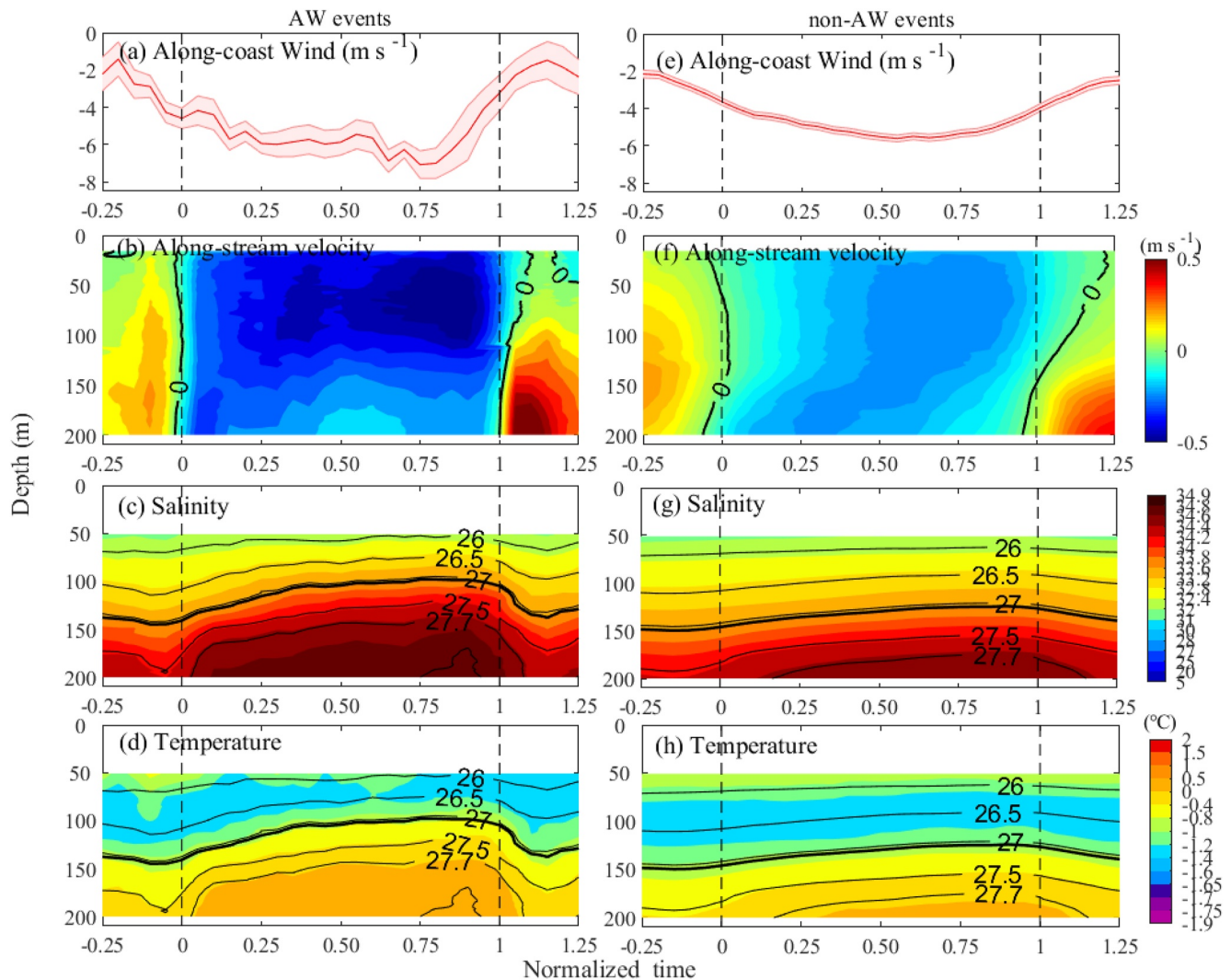
Figure 8. Composite events of the Atlantic Water (AW) upwelling (left column) and the non-AW upwelling (right column). (a and e) Along-coast wind speed (m s^{-1}) where negative is northeasterly. The shading represents standard error. (b and f) Depth-dependent along-stream current velocity (m s^{-1}) where negative is up-canyon, the 0 contour is highlighted. (c and g) Salinity and (d and h) potential temperature (°C), overlain by potential density (kg m^{-3}). The thick contour represents the interface of Pacific Water and Atlantic Water (27.06 kg m^{-3} isopycnal).

same level as the beginning. Similar to the AW upwelling, the outflow is reversed during the event, but with a much weaker velocity (Figure 8f). It is again followed by a rebound jet. In this case the Pacific Water-AW interface is only 20 m above the background 150 m (Figure 8h).

5. Impact of Upwelling on Ice Cover

Upwelling in Barrow Canyon can develop polynyas in the cold season via wind-driven ice divergence and/or oceanic heating, however these two mechanisms are difficultly distinguished (Hirano et al., 2016; Ladd et al., 2016). Using the timeseries of the spatially averaged ice concentration in the vicinity of Barrow Canyon (orange box in Figure 1a), we first identified the ice period for each year (September to next August) as the time between the freeze-up date when the ice concentration first exceeded 90% and melt-back date when the ice concentration last dropped below 90% (Tian et al., 2021). We found there are 150 upwelling events in the ice period (328 events in total), including 11 AW upwelling events, 125 non-AW upwelling events and 14 50%-chance AW upwelling events. Remind that the AW and non-AW upwelling events were identified by UI, based on the shorter record when BC2 was operating. We aim to address how the AW upwelling plays a role in modulating the
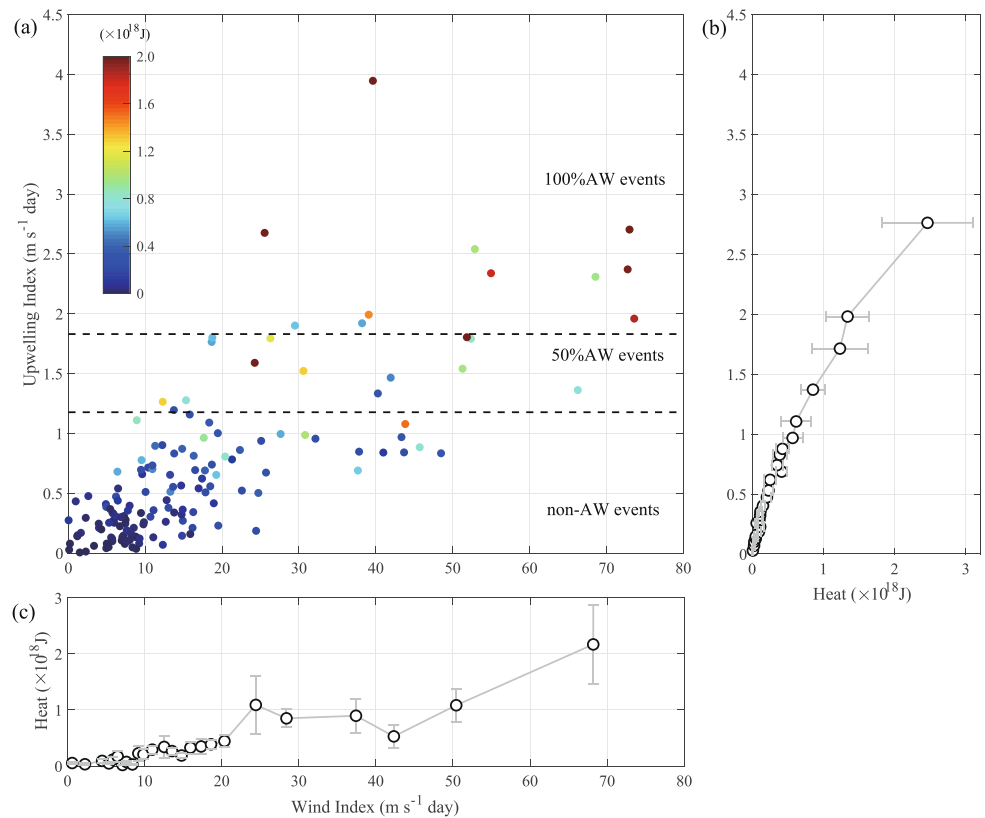
Figure 9. (a) Upwelling index (UI) versus wind index for the 150 upwelling events in the ice period, colored by the cumulated heat (J). The thresholds of Atlantic Water (AW) upwelling events and non-AW events are denoted by two black dashed lines. (b) Averaged cumulated heat for each bin of UI. (c) Averaged cumulated heat for each bin of wind index. Standard errors are included.

ice cover versus the non-AW upwelling, and to shed further light on the two mechanisms, wind divergence and oceanic heating. We focus on the 150 events in ice period in the following analysis.

For each of the two types of upwelling, we computed the cumulated heat (H) that is fluxed up-canyon (see Section 2.6 for the details). Figure 9a shows the scatter plot of WI versus UI colored by the cumulated heat for the upwelling events in the ice period. Not surprisingly, the AW upwelling generally transports more heat than the non-AW upwelling, with mean values of 1.9×10^{18} J versus 0.2×10^{18} J. Each of the AW events transports over 1×10^{18} J heat except for two events with the weaker upwelling strength (UI < 2) fluxing ~0.8×10^{18} J, which are still much higher than the mean heat during non-AW upwelling. To further clarify the relation of the upwelling strength and the heat transport, we averaged the cumulated heat with each bin of UI (each bin contains six data points, so that the bin size increases as the UI increases). It reveals that stronger upwelling transports more heat up-canyon (Figure 9b). Analogously, we also averaged the cumulated heat for each bin of WI (Figure 9c). It shows that the cumulated heat increases as the wind intensifies. This causes the difficulty of teasing apart their effects on ice loss.

We now investigate the impact of AW upwelling versus non-AW upwelling on the ice cover of the Chukchi Sea shelf. To isolate the effect of wind, we chose the AW upwelling and non-AW upwelling events that have a similar WI (50%-chance AW events were not considered here). Since AW upwelling is generally associated with the stronger wind (higher WI) than non-AW upwelling (Figure 9a), we can only find two WI bins including both types of the upwelling (Figures 10a and 10c): 25–30 and 36–41 m s^{-1} day.

In the first wind scenario (WI = 25–30 m s^{-1} day), there are two AW events and three non-AW events (Figure 10a). During each of these events, the ice concentration decreases with a large variation. In addition, there are discrepancies between the events, such as the time of onset of the ice decrease due to different delay responses. To better compare, we first found the minimum value of the ice concentration during each upwelling event, and considered
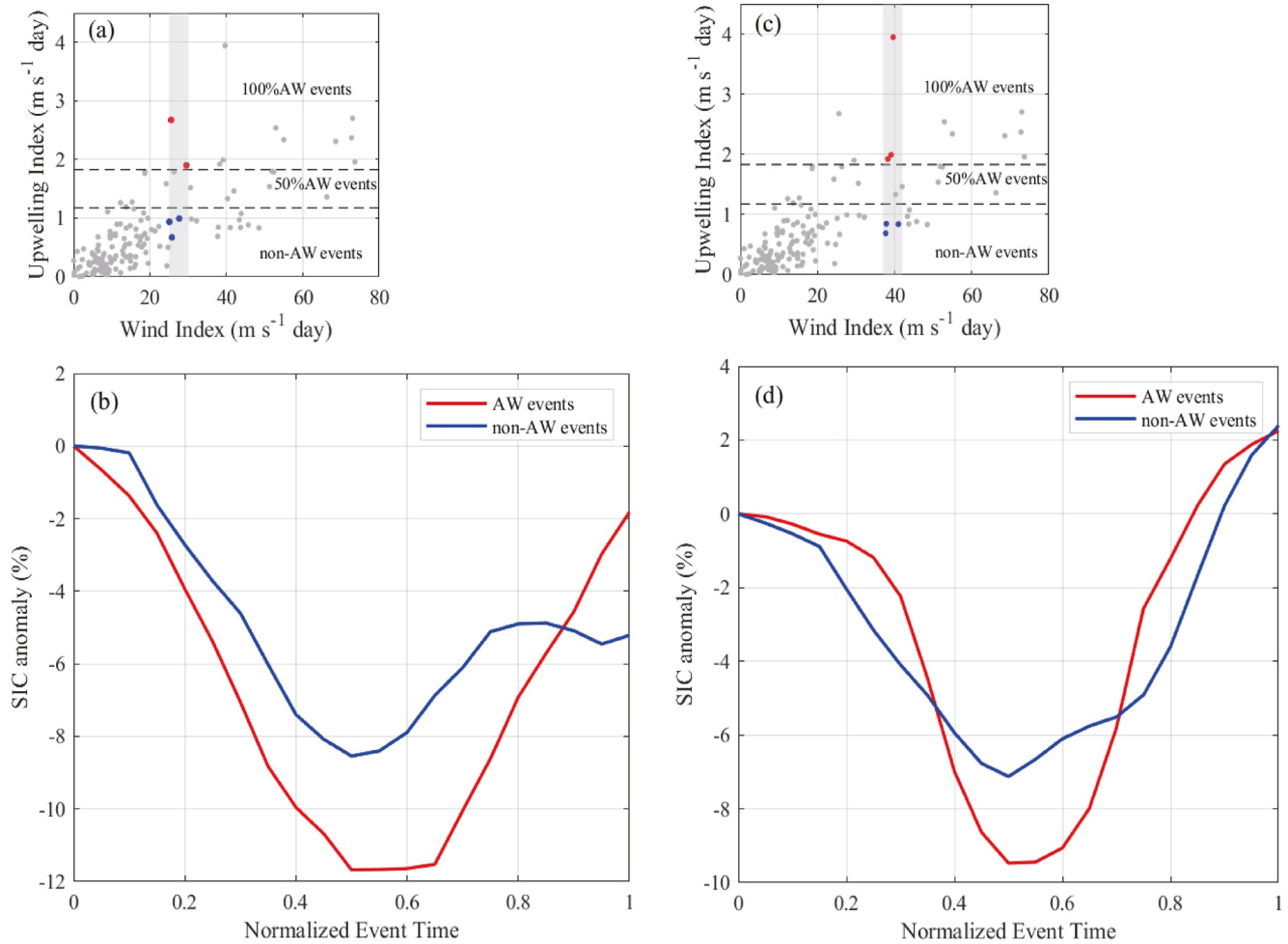
Figure 10. (a) The selected Atlantic Water (AW) upwelling events (red dots) and non-AW upwelling events (blue dots) when WI is in the range of 25–30 m s^{-1} day. All upwelling events in the ice period are marked by gray dots. (b) Composites of ice concentration anomaly for the selected AW events (red curve) and non-AW events (blue curve). (c and d) are the same to (a and c), respectively, except for the wind scenario of WI = 36–41 m s^{-1} day.

the first peak of the ice concentration backwards as the initial ice condition before influenced by upwelling. Note that ice starts decreasing after the onset of upwelling. Figure 10b presents the composites of the ice concentration anomalies from the initial ice cover during a normalized period (different to the normalized upwelling period), $t_n = 0$ at the time of onset of ice reduction and $t_n = 0.5$ at the time of the minimum ice. It reveals that the ice declines ~12% during the AW events versus ~8% during the non-AW events. Note that in this wind scenario, on average the AW upwelling events transport 1.5×10^{18} J heat, while the non-AW upwelling events transport 0.38×10^{18} J.

In the other wind scenario (WI = 36–41 m s^{-1} day), we identified three AW events (1.4×10^{18} J), causing ~10% ice decrease, and three non-AW events (0.36×10^{18} J) when the ice concentration was reduced by ~7% (Figures 10c and 10d). We thus argue that under a similar wind forcing, the more ice decrease in the AW upwelling events than that in the non-AW upwelling events is due to the influence of the extra heat carried by the warm AW. It is further addressed below.

What is the spatial change of the ice cover during the upwelling? We used the upwelling events with WI = 25–30 m s^{-1} day as an example (the results are similar for the other wind scenario). For each type of the upwelling events, we constructed maps of the ice concentration in the initial condition and when the mean ice reaches the minimum, and the difference (Figure 11). The initial ice condition is similar for both types of upwelling, the study region is fully ice covered except for the coastal region where the ice concentration is around 90% (Figures 11a and 11b). Figure 11c reveals the in non-AW upwelling, reduction of the ice occurs confined
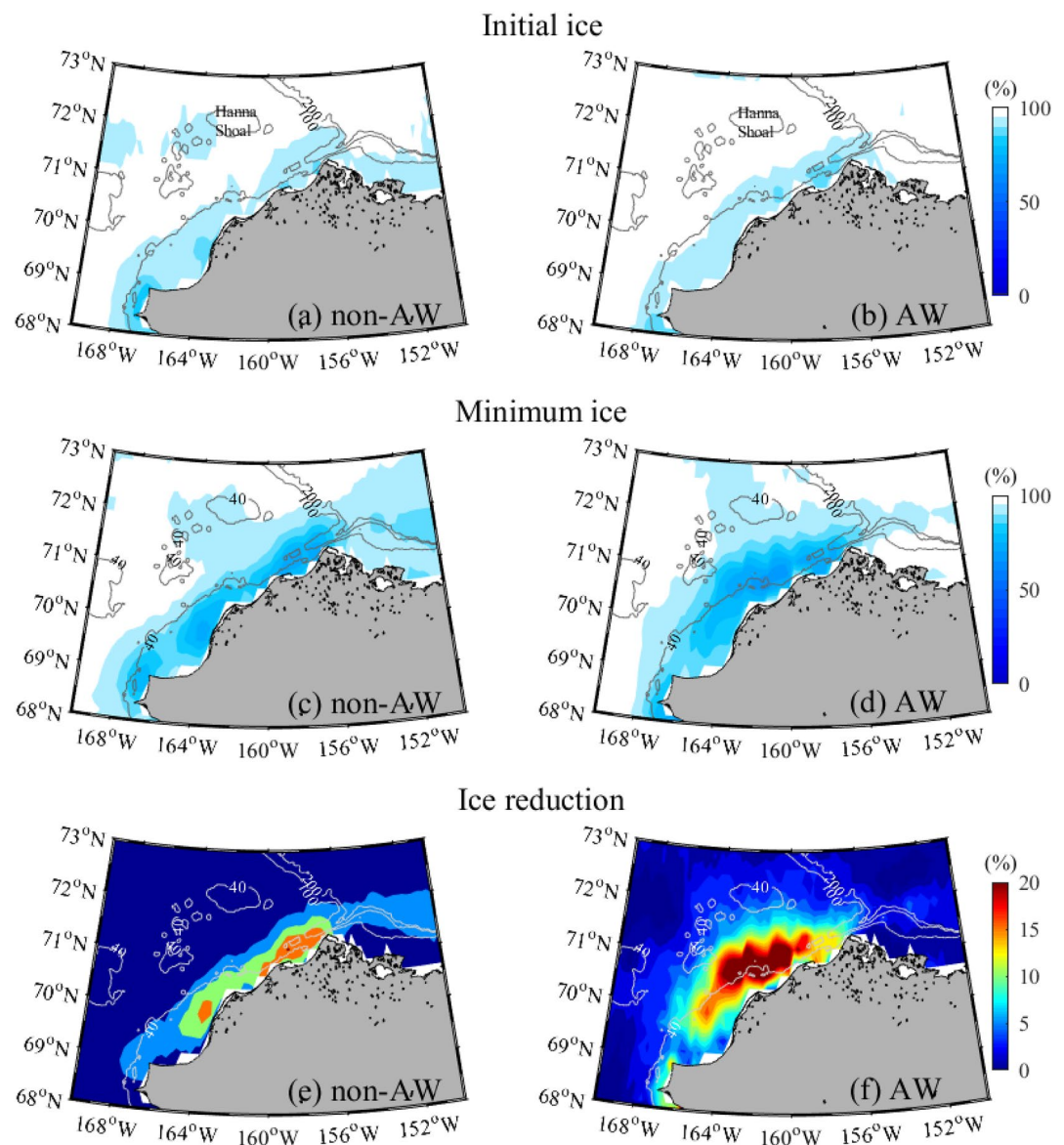
Figure 11. Composites of (a and b) initial ice condition, (c and d) minimum ice condition and (e and f) ice reduction in the non-Atlantic Water (AW) upwelling (left column) and the AW upwelling (right column), when WI is in 25–30 m s^{-1} day. The gray contours are the isobaths of 40, 100, and 200 m.

to the coastal region. The band of large ice reduction adjoins to the Alaskan coast from Barrow Canyon to 69°N (Figure 11e). In contrast, in AW upwelling, the minimum ice condition shows ice decreases in the coastal region and also in the interior, south of the Hanna Shoal (Figure 11d). The significant ice reduction appears in the south of the Hanna Shoal, away from the coast (Figure 11f). Note that the kinematic effect of along-coast wind (wind-driven divergence of ice) takes place within the coastal region, and during the upwelling events wind stress curl is negative in the shelf interior which is also not favorable to the polynya formation. The up-canyon flux of heat by AW upwelling would be available for melting approximately 4,900 km^2 of 1 m thick ice on the Chukchi Sea shelf, consistent with the area of ice loss, 5,300 km^2 (ice concentration deceases more than 10%, Figure 11f). In contrast, the heat brought by non-AW upwelling can only melt 1,300 km^2. More importantly, it is far less than the real ice-loss area, 2,800 km^2 (Figure 11e). These results demonstrate that (a) the ice decrease during non-AW upwelling is mainly driven by the wind-driven divergence, and (b) the oceanic heating plays a dominant role in the ice reduction during the AW upwelling which brings a large amount of heat up to the shelf.
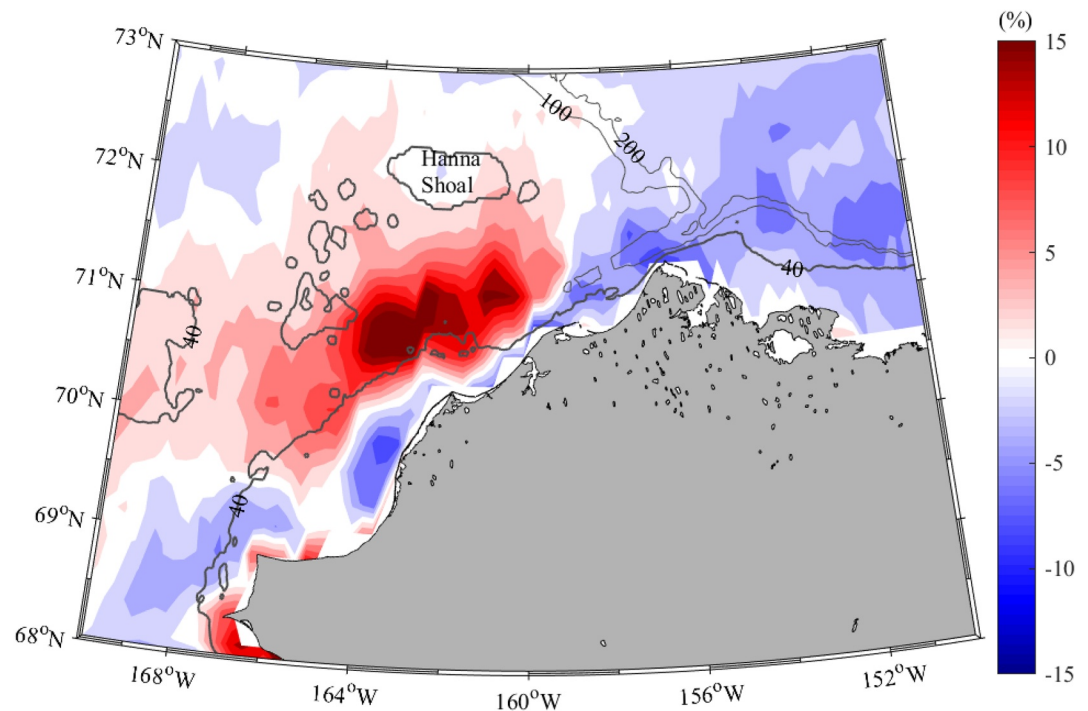
Figure 12. Difference of the ice reduction in the Atlantic Water (AW) upwelling versus the non-AW upwelling (Figures 11e and 11f).

As such, the difference of the ice reduction between the two types of upwelling to some degree reflects the effect of heat (Figure 12). The major difference between the two cases is seen on the shelf offshore of the 40 m isobath (positive values), consistent with the region where Ladd et al. (2016) observed the AW signal. It indicates that during the AW upwelling, the fluxed heat (1.1×10^{18} J more than that during the non-AW upwelling) can reduce ~15% more ice in the shelf interior.

6. Discussion

Only a few events went into each of the composites and there are considerable variances between the events for each wind scenario. These to some degree weaken the statistical significance of our results. Nonetheless, we found the consistency in two different wind scenarios—the more ice is reduced in the Chukchi shelf in the AW upwelling events than in the non-AW events (Figure 10). The spatial distributions of ice reduction are consistent with the results of Ovall et al. (2021) who performed an empirical orthogonal function (EOF) analyses of ice cover in the same study area. Their EOF mode 1 reveals the regions of ice reduction adjacent to the coast, reflecting a wind-driven polynya, while the mode 2 shows the ice reduces from the head of Barrow Canyon toward the shelf interior, representing the melt-driven polynya from oceanic heat flux. These are in line with our arguments of the ice reduction in the non-AW events versus the AW events respectively in this study.

Our result clearly suggests that when wind is constant, more heat flux is more likely to melt ice. Note that the actual heat for melting ice may be less than the total heat brought by the upwelling in the mouth of Barrow Canyon shown above. It is due to multiple factors such as heat loss on the way approaching the shelf, and stratification of the water column. However, observations of the stratification in water column during an upwelling in the ice period are rare. Using a mooring at the head of Barrow Canyon, Hirano et al. (2016) found that during an upwelling the temperature dramatically increase in the bottom as well as in the mid-layer. A numerical tracer study by Hirano et al. (2018) revealed that the AW signal appears in the surface extending from the coastal region of northeastern Chukchi Sea to the shelf interior. These are consistent with the areas of significant ice reduction during AW upwelling in our study (Figure 12).

7. Conclusions

Using 12 years of mooring data, together with the weather station data and satellite ice concentration data, we investigated the general characteristics of upwelling, particularly the upwelling of AW, in Barrow Canyon and the impacts on the ice cover of the Chukchi Sea shelf. Based on the criteria of reversed (up-canyon) velocity and northeasterly wind, we identified 328 upwelling events over the 12-year record. More upwelling occurs in the cold months, and the occurrence of the upwelling appears to have an increase trend since 2001, associated with the variations of the strong northeasterly winds. To characterize the upwelling, we constructed a composite event by normalizing the time period of each event from 0 to 1. It reveals that as the northeasterly wind intensifies, the along-stream current reverses to up-canyon and the upwelling commences, revealed by the raising upper boundary of warm and salty AW. After the upwelling, a rebound flow is established in the lower layer. We quantified the relation of the upwelling and the along-coast wind by regressing the UI and WI. It shows a significant correlation ($R = 0.75$, $p < 0.01$), indicating that the stronger northeasterly winds drive more intense upwelling, which is consistent with the previous studies.

Employing a 4-year hydrographic data set at the bottom of the mooring near the head of Barrow Canyon, we examined the occurrence of AW on the shelf during upwelling events. It suggests that the extreme upwelling events (UI > 1.83) and a half of the medium events (1.18 < UI < 1.83) can bring the AW to the head of canyon, while the remaining are the non-AW events (UI < 1.18). We applied the thresholds to all identified upwelling in the 12 years, and found 22 AW upwelling, 283 non-AW upwelling, and 23 events with half the chance of bringing AW. Upwelling of AW mainly occurs in the cold months. In contrast, the non-AW upwelling occurs throughout the year, and have more occurrence and stronger strength in the cold months. There is no significant interannual trend in both types of the upwelling. These variations of upwelling are mainly associated with the northeasterly winds. During the AW events, under a stronger wind the reversed current is more intensified with the core in the sub-surface. At the mouth of the canyon, the upper boundary of the AW was vertically uplifted by 50 m from the background condition, while only by 20 m in the non-AW events.

We analyzed 150 upwelling events in the ice periods to explore the impact of upwelled AW on ice loss in the study region. In general, stronger upwelling can flux more heat up-canyon, particularly in the AW upwelling events. Under similar wind forcing (similar WI), the AW upwelling is associated with more ice reduction than the non-AW upwelling. The ice loses the most along the coast during the non-AW upwelling, while during the AW upwelling reduces more ice in the shelf interior, away from the coast. The AW upwelling results in up to 15% more ice reduction in the shelf interior than the non-AW upwelling, caused by the large amount of heat fluxed onto the shelf.

Our analyses of 12 years of data provide guidance as to the relative effects of wind divergence and oceanic heat flux on the ice cover in the northeastern Chukchi Sea. These outcomes suggest methods for assessing likely impacts on Chukchi Sea ice distributions in future climates, using modeled changes in winds to identify whether AW upwelling is more or less likely to occur in future. Furthermore, this research motivates us to address the implications for the biological processes during the AW upwelling events in the future.

Data Availability Statement

The data of the three moorings at the mouth of Barrow Canyon are provided by JAMSTEC (http://www.jamstec.go.jp/arctic/). The hydrographic data at the mooring BC2 near the head of the canyon are available at National Oceanographic Data Center (NODC, https://www.nodc.noaa.gov/archive/arc0113/0160090/). Wind data from the meteorological station in Utqiaġvik, AK are available at https://www.ncdc.noaa.gov/cdo-web/datasets/GHCND/stations/GHCND:USW00027502/detail. The AVHRR sea ice concentration data are available at https://www.ncei.noaa.gov/data/sea-surface-temperature-optimum-interpolation/v2.1/access/avhrr/.

References

Aagaard, K., & Roach, A. T. (1990). Arctic ocean-shelf exchange: Measurements in Barrow Canyon. *Journal of Geophysical Research*, *95*(C10), 18163–18175. https://doi.org/10.1029/JC095iC10p18163

Aksenov, Y., Ivanov, V. V., Nurser, A. J. G., Bacon, S., Polyakov, I. V., Coward, A. C., et al. (2011). The Arctic circumpolar boundary current. *Journal of Geophysical Research*, *116*(C9). https://doi.org/10.1029/2010JC006637

Beaird, N. L., Shroyer, E. L., Juranek, L. W., Hales, B., & Goñi, M. A. (2020). Nutrient-rich gravity current formed by upwelling in Barrow Canyon: High-resolution observations. *Journal of Geophysical Research: Oceans*, *125*(7), e2020JC016160. https://doi.org/10.1029/2020JC016160

Carmack, E. C., & Kulikov, E. A. (1998). Wind-forced upwelling and internal Kelvin wave generation in Mackenzie Canyon, Beaufort Sea. *Journal of Geophysical Research*, *103*(C9), 18447–18458. https://doi.org/10.1029/98jc00113

Gong, D., & Pickart, R. S. (2016). Early summer water mass transformation in the eastern Chukchi Sea. *Deep Sea Research Part II: Topical Studies in Oceanography*, *130*, 43–55. https://doi.org/10.1016/j.dsr2.2016.04.015

Grebmeier, J. M., Bluhm, B. A., Cooper, L. W., Danielson, S. L., Arrigo, K. R., Blanchard, A. L., et al. (2015). Ecosystem characteristics and processes facilitating persistent macrobenthic biomass hotspots and associated benthivory in the Pacific Arctic. *Progress in Oceanography*, *136*, 92–114. https://doi.org/10.1016/j.pocean.2015.05.006

Grebmeier, J. M., Cooper, L. W., Feder, H. M., & Sirenko, B. I. (2006). Ecosystem dynamics of the Pacific-influenced northern Bering and Chukchi Seas in the Amerasian Arctic. *Progress in Oceanography*, *71*(2), 331–361. https://doi.org/10.1016/j.pocean.2006.10.001

Hirano, D., Fukamachi, Y., Ohshima, K. I., Watanabe, E., Mahoney, A. R., Eicken, H., et al. (2018). Winter water formation in coastal polynyas of the eastern Chukchi shelf: Pacific and Atlantic influences. *Journal of Geophysical Research: Oceans*, *123*, 5688–5705. https://doi.org/10.1029/2017JC013307

Hirano, D., Fukamachi, Y., Watanabe, E., Ohshima, K. I., Iwamoto, K., Mahoney, A. R., et al. (2016). A wind-driven, hybrid latent and sensible heat coastal polynya off Barrow, Alaska. *Journal of Geophysical Research: Oceans*, *121*. https://doi.org/10.1002/2015jc011318

Itoh, M., Nishino, S., Kawaguchi, Y., & Kikuchi, T. (2013). Barrow Canyon volume, heat, and freshwater fluxes revealed by long-term mooring observations between 2000 and 2008. *Journal of Geophysical Research: Oceans*, *118*(9), 4363–4379. https://doi.org/10.1002/jgrc.20290

Itoh, M., Pickart, R. S., Kikuchi, T., Fukamachi, Y., Ohshima, K. I., Simizu, D., et al. (2015). Water properties, heat and volume fluxes of Pacific water in Barrow Canyon during summer 2010. *Deep Sea Research Part I: Oceanographic Research Papers*, *102*, 43–54. https://doi.org/10.1016/j.dsr.2015.04.004

Itoh, M., Shimada, K., Kamoshida, T., McLaughlin, F., Carmack, E., & Nishino, S. (2012). Interannual variability of Pacific winter water inflow through Barrow canyon from 2000 to 2006. *Journal of Oceanography*, *68*(4), 575–592. https://doi.org/10.1007/s10872-012-0120-1

Ladd, C., Mordy, C. W., Salo, S. A., & Stabeno, P. J. (2016). Winter water properties and the Chukchi polynya. *Journal of Geophysical Research: Oceans*, *121*(8), 5516–5534. https://doi.org/10.1002/2016jc011918

Li, J., Lin, P., Pickart, R. S., & Yang, X.-Y. (2021). Time dependent flow of Atlantic water on the continental slope of the Beaufort Sea based on moorings. *Journal of Geophysical Research: Oceans*, *126*(6), e2020JC016996. https://doi.org/10.1029/2020JC016996

Li, J., Pickart, R. S., Lin, P., Bahr, F., Arrigo, K. R., Juranek, L., & Yang, X.-Y. (2020). The Atlantic water boundary current in the Chukchi Borderland and southern Canada basin. *Journal of Geophysical Research: Oceans*, *125*(8), e2020JC016197. https://doi.org/10.1029/2020JC016197

Lin, P., Pickart, R. S., Fissel, D., Ross, E., Kasper, J., Bahr, F., et al. (2020). Circulation in the vicinity of Mackenzie Canyon from a year-long mooring array. *Progress in Oceanography*, *187*, 102396. https://doi.org/10.1016/j.pocean.2020.102396

Lin, P., Pickart, R. S., Mcraven, L. T., Arrigo, K. R., Bahr, F., Lowry, K. E., et al. (2019). Water mass Evolution and circulation of the northeastern Chukchi Sea in summer: Implications for nutrient distributions. *Journal of Geophysical Research: Oceans*, *124*(7). https://doi.org/10.1029/2019jc015185

Lin, P., Pickart, R. S., Moore, G., Spall, M. A., & Hu, J. (2019). Characteristics and dynamics of wind-driven upwelling in the Alaskan Beaufort Sea based on six years of mooring data. *Deep Sea Research Part II: Topical Studies in Oceanography*, *162*, 79–92. https://doi.org/10.1016/j.dsr2.2018.01.002

Lin, P., Pickart, R. S., Stafford, K. M., Moore, G. W. K., Torres, D. J., Bahr, F., & Hu, J. (2016). Seasonal variation of the Beaufort shelf-break jet and its relationship to Arctic cetacean occurrence. *Journal of Geophysical Research: Oceans*, *121*(12), 8434–8454. https://doi.org/10.1002/2016jc011890

Lin, P., Pickart, R. S., Vage, K., & Li, J. (2021). Fate of warm Pacific water in the Arctic basin. *Geophysical Research Letters*, *48*, e2021GL094693. https://doi.org/10.1029/2021gl094693

Macdonald, R. W., Wong, C. S., & Erickson, P. E. (1987). The distribution of nutrients in the southeastern Beaufort Sea: Implications for water circulation and primary production. *Journal of Geophysical Research*, *92*(C3), 2939–2952. https://doi.org/10.1029/jc092ic03p02939

National Geophysical Data Center. (2006). *2-minute Gridded Global Relief Data (ETOPO2) v2*. NOAA National Centers for Environmental Information. https://doi.org/10.7289/V5J1012Q

Nikolopoulos, A., Pickart, R. S., Fratantoni, P. S., Shimada, K., Torres, D. J., & Jones, E. P. (2009). The western Arctic boundary current at 152°W: Structure, variability, and transport. *Deep Sea Research Part II: Topical Studies in Oceanography*, *56*(17), 1164–1181. https://doi.org/10.1016/j.dsr2.2008.10.014

Okkonen, S. R., Ashjian, C. J., Campbell, R. G., Maslowski, W., Clement-Kinney, J. L., & Potter, R. (2009). Intrusion of warm Bering/Chukchi waters onto the shelf in the western Beaufort Sea. *Journal of Geophysical Research*, *114*(C1). https://doi.org/10.1029/2008JC004870

Ovall, B., Pickart, R. S., Lin, P., Stabeno, P., Weingartner, T., Itoh, M., et al. (2021). Ice, wind, and water: Synoptic-scale controls of circulation in the Chukchi Sea. *Progress in Oceanography*, *199*, 102707. https://doi.org/10.1016/j.pocean.2021.102707

Pawlowicz, R., Beardsley, B., & Lentz, S. (2002). Classical tidal harmonic analysis including error estimates in MATLAB using T_TIDE. *Computers & Geosciences*, *28*(8), 929–937. https://doi.org/10.1016/s0098-3004(02)00013-4

Pickart, R. S., Nobre, C., Lin, P., Arrigo, K. R., Ashjian, C. J., Berchok, C., et al. (2019). Seasonal to mesoscale variability of water masses and atmospheric conditions in Barrow Canyon, Chukchi Sea. *Deep Sea Research Part II: Topical Studies in Oceanography*, *162*, 32–49. https://doi.org/10.1016/j.dsr2.2019.02.003

Pickart, R. S., Schulze, L. M., Moore, G. W. K., Charette, M. A., Arrigo, K. R., van Dijken, G., & Danielson, S. L. (2013). Long-term trends of upwelling and impacts on primary productivity in the Alaskan Beaufort Sea. *Deep Sea Research Part I: Oceanographic Research Papers*, *79*, 106–121. https://doi.org/10.1016/j.dsr.2013.05.003

Pickart, R. S., Spall, M. A., Lin, P., Bahr, F., McRaven, L. T., Arrigo, K. R., & Grebmeier, J. M. (2021). Physical controls on the macrofaunal benthic biomass in Barrow Canyon, Chukchi Sea. *Journal of Geophysical Research: Oceans*, *126*(5), e2020JC017091. https://doi.org/10.1029/2020JC017091

Pickart, R. S., Spall, M. A., & Mathis, J. T. (2013). Dynamics of upwelling in the Alaskan Beaufort Sea and associated shelf–basin fluxes. *Deep Sea Research Part I: Oceanographic Research Papers*, *76*, 35–51. https://doi.org/10.1016/j.dsr.2013.01.007

Pickart, R. S., Spall, M. A., Moore, G. W. K., Weingartner, T. J., Woodgate, R. A., Aagaard, K., & Shimada, K. (2011). Upwelling in the Alaskan Beaufort Sea: Atmospheric forcing and local versus non-local response. *Progress in Oceanography*, *88*(1–4), 78–100. https://doi.org/10.1016/j.pocean.2010.11.005

Pisareva, M. N., Pickart, R. S., Lin, P., Fratantoni, P. S., & Weingartner, T. J. (2019). On the nature of wind-forced upwelling in Barrow Canyon. *Deep Sea Research Part II: Topical Studies in Oceanography*, *162*, 63–78. https://doi.org/10.1016/j.dsr2.2019.02.002

Proshutinsky, A., Krishfield, R., Timmermans, M. L., Toole, J., Carmack, E., Mclaughlin, F., et al. (2009). Beaufort Gyre freshwater reservoir: State and variability from observations. *Journal of Geophysical Research*, *114*, C00A10. https://doi.org/10.1029/2008jc005104

Reynolds, R. W., Smith, T. M., Liu, C., Chelton, D. B., Casey, K. S., & Schlax, M. G. (2007). Daily high-resolution-blended analyses for sea surface temperature. *Journal of Climate*, *20*(22), 5473–5496. https://doi.org/10.1175/2007jcli1824.1

Schulze, L. M., & Pickart, R. S. (2012). Seasonal variation of upwelling in the Alaskan Beaufort Sea: Impact of sea ice cover. *Journal of Geophysical Research*, *117*(C6). https://doi.org/10.1029/2012jc007985

Tian, F., Pickart, R. S., Lin, P., Pacini, A., Moore, G. W. K., Stabeno, P., et al. (2021). Mean and seasonal circulation of the eastern Chukchi Sea from moored timeseries in 2013–2014. *Journal of Geophysical Research: Oceans*, *126*(5), e2020JC016863. https://doi.org/10.1029/2020JC016863

Weingartner, T., Aagaard, K., Woodgate, R., Danielson, S., Sasaki, Y., & Cavalieri, D. (2005). Circulation on the north central Chukchi Sea shelf. *Deep Sea Research Part II: Topical Studies in Oceanography*, *52*(24), 3150–3174. https://doi.org/10.1016/j.dsr2.2005.10.015

Weingartner, T., Potter, R. A., Stoudt, C. A., Dobbins, E. L., Statscewich, H., Winsor, P. R., et al. (2017). Transport and thermohaline variability in Barrow Canyon on the northeastern Chukchi Sea shelf. *Journal of Geophysical Research: Oceans*, *122*, 3565–3585. https://doi.org/10.1002/2016jc012636

Woodgate, R. A. (2018). Increases in the Pacific inflow to the Arctic from 1990 to 2015, and insights into seasonal trends and driving mechanisms from year-round Bering Strait mooring data. *Progress in Oceanography*, *160*, 124–154. https://doi.org/10.1016/j.pocean.2017.12.007